ROYAL SOCIETY OF CHEMISTRY

PAPER

Check for updates

Stretchable separator/current collector composite for superior battery safety†

Zhikang Liu,‡[a] Yanhao Dong, ‡[b] Xiaoqun Qi,[c] Ru Wang,[ade] Zhenglu Zhu,[a] Chao Yan,[de] Xinpeng Jiao,[e] Sipei Li,[b] Long Qie,*[c] Ju Li *[bf] and Yunhui Huang *[c]

Safety is the most concerning issue for high-energy-density batteries. Here we show how mechanical abuse-induced short-circuiting can be mitigated by designing a structure of highly deformable separator/current collector (SCC) composite that wraps around broken edges and electronically insulates them upon penetration. We report progress in roll-to-roll processed metalized plastic SCC, where 750 nm thick nanocrystalline aluminum deposited on 6 μm polyethylene terephthalate (PET) substrate is used to replace 14 μm Al foil as the current collector (CC) in rechargeable lithium-ion batteries (LIBs). The Al–PET SCC nanocomposite not only increases the cell-level energy density by lowering CC's thickness and weight, but also dramatically increases the battery safety in harsh mechanical penetration accidents. The improved safety is due to better mechanical ductility of PET than Al and cathode, such that in penetration, the insulating PET can extend and isolate around the broken edges and the cathode can be automatically delaminated and insulated from the external circuit, thus preventing short-circuiting induced thermal runaway.

Broader context

The surge of the electric vehicles (EVs) drives people to seek out advanced batteries with higher energy density and better safety. While the approaches to increase the energy density of lithium-ion batteries (LIBs), *i.e.*, using high-specific-capacity electrode materials like high-nickel NCM ($LiNi_{1−x−y}Co_xMn_yO_2$) cathodes or Si-based anodes, always bring new safety concerns. Herein, we reported an advanced technology to construct LIBs with higher energy density and superior safety. Al-deposited polyethylene terephthalate (PET) was prepared *via* a roll-to-roll mass production and used to replace commercial Al foil as the current collectors and as the accident-active "separator" during mechanically abused events. Compared with the state-of-the-art 14 μm Al current collectors, the as-designed separator/current collector (SCC) composite shows competing mechanical and electrical properties, while reducing 70.4% weight, 46.4% volume and 89.3% metal usage without sacrificing any major battery performance. Remarkably, the use of SCC dramatically improves the safety of the fully-charged pouch cells using $LiNi_{0.8}Co_{0.1}Mn_{0.1}O_2$ cathode and hybrid graphite@SiO anode in harsh nail penetration and impact tests. This work provides a practical solution to superior battery safety, which might be universally applicable to other battery chemistries.

[a] *Institute of New Energy for Vehicles, School of Materials Science and Engineering, Tongji University, Shanghai 201804, China*

[b] *Department of Nuclear Science and Engineering, Massachusetts Institute of Technology, Cambridge, MA 02139, USA. E-mail: liju@mit.edu*

[c] *State Key Laboratory of Material Processing and Die & Mold Technology, School of Materials Science and Engineering, Huazhong University of Science and Technology, Wuhan, Hubei 430074, China. E-mail: qie@hust.edu.cn, huangyh@hust.edu.cn*

[d] *Nanjing Tongning Institute of New Materials, Nanjing, Jiangsu 211161, China*

[e] *Zhejiang Rouzhen Technology Co., Ltd., Jiaxing, Zhejiang 314499, China*

[f] *Department of Materials Science and Engineering, Massachusetts Institute of Technology, Cambridge, MA 02139, USA*

† Electronic supplementary information (ESI) available. See DOI: https://doi.org/10.1039/d2ee01793h

‡ These authors contributed equally.

Introduction

Green energy calls for lithium-ion batteries (LIBs) with higher energy density and better safety.[1–3] It pushes all battery components to their limits, including electrochemically inactive ones. One such example is the current collector (CC), whose thickness (thus weight) has been dramatically reduced from 20 μm for Cu (CC for anodes; density: 8.96 g cm^{-3}) and 18 μm for Al (CC for cathodes; density: 2.70 g cm^{-3}) in the 1990s to the state-of-the-art 6–10 μm for Cu and 10–15 μm for Al *via* processing optimizations.[4–7] This reduces the materials cost and increases the cell-level energy density. However, further lowering metallic CC's thickness is technologically challenging (especially to achieve good surface finish, homogeneity, and

This journal is © The Royal Society of Chemistry 2022

Energy Environ. Sci., 2022, **15**, 5313–5323 | 5313

reproducibility for roll-to-roll production) and complicates handling in battery assembly and operation.[8,9] New strategies are required to innovate CC design and processing. Some novel CC designs have been proposed in the literature, especially to enhance electrode-level electronic transport in high-rate batteries. Examples include graphene foams,[10–12] reduced oxide graphene films,[13–15] porous metal scaffolds,[16–18] and metallic meshes.[19,20] But these designs generally have high surface areas, poor mechanical properties, high cost, and poor compatibility with roll-to-roll processing.

Metallized plastic films have been widely used as decoration,[21,22] packaging,[23,24] and insulation materials,[25,26] including aluminum laminated films for pouch cell casing.[27] These metallized films are typically produced by physical vapor deposition techniques, where metal (Al being the most frequently used one) is thermally evaporated on large-area polymer films.[28,29] The deposited metal layer with 0.05–0.5 μm thickness offers a reflective silvery/metallic surface and reduces the permeability to light, water and oxygen.[30] In recent years, the battery community has sought double-sided metallized plastic films as CCs, with reduced weight, volume, and metal usage to substitute purely metallic Cu/Al CCs.[31,32] In academic literature, Cui *et al.* recently reported light-weight metallized plastic CCs such as Cu coated polyimide (Cu-PI) anode CCs, where fire retardants were added to improve battery safety.[33] However, it remains an open question whether the large-scale roll-to-roll processed metallized plastic CCs can have comparable properties to metallic CCs and whether they be readily used in large-capacity pouch cells.

Regarding battery safety, it is well known that thermal runaway is a complex, self-accelerating, chain-reaction-like event.[34,35] Charged batteries under electrically, thermally, or mechanically abused conditions may undergo a chain reaction, which may initially start from a small region and eventually explode. (See Video S1 for the violent explosion during the nail penetration test of a fully charged 4.3 A h pouch cell using $LiNi_{0.8}Co_{0.1}Mn_{0.1}O_2$ cathode and hybrid graphite@SiO anode. ESI†) It raises safety concerns in energy-dense LIBs, as flammables (*e.g.*, organic electrolytes and polymer separators) and oxidants (*e.g.*, charged cathodes) are both available inside the cell.[36–38] This could be especially problematic for high-energy-density LIBs (*e.g.*, using Ni-rich layered oxide cathodes with ultra-high Ni content and high upper-cutoff voltage,[39–42] because they can easily release reactive oxygen singlets/molecules upon heating[43,44]) used in electric vehicles (EVs). The average motorist experiences about 4 car accidents in his/her life.[45] Even for low-speed collisions with stationary obstacles at 30 miles per hour, the mechanical integrity of the EV battery pack cannot be guaranteed,[46] and there is a significant chance for breaching of the battery cell packaging by external penetrants. Therefore, it would be valuable to design a new cathode CC that can automatically cut down electrical contact of mechanically abused cathodes from LIB electronic pathway and increase battery safety by addressing the cathode-side issue (*i.e.*, minimizing oxidants of the exothermic reactions).

In this work we show that battery safety can be dramatically improved by a system-level design of utilizing multilayer

separator/current collector (SCC) composite to replace all-metallic CCs, without sacrificing energy density. The rationale for this design is the following. Traditional LIBs consist of periodic stacking of five layers: Cu CC (6–10 μm), Al CC (10–15 μm), anode-active layer (AAL, ~70 μm), cathode-active layer (CAL, ~70 μm), and a microporous separator (MPS) layer usually made of polypropylene or polyethylene (~10 μm). All the layers except MPS are good electronic conductors (conductive agents are intentionally added to CAL to improve electronic percolation). Thus, out of any ~170 μm period, only ~5% (*i.e.*, the MPS layer) is electronically insulating. The MPS is also porous and fragile and it shrinks upon heating, further decreasing the electronically insulating fraction. Despite best efforts to improve its thermomechanical robustness, AAL dendrites, CAL surface asperities or metallic-dust penetrants, heat-induced shrinkage, short overhangs *etc.*[47] of the MPS are the key reasons for battery safety failures (*i.e.*, Samsung Galaxy Note 7), even without any external mechanical insult. There is a general lack of "separator power" since the battery cell internals are mostly electronically conductive, so when there is an external penetrant that induces deformation and offsetting of the layers, it is very easy for different conductive parts to be no longer electronically insulated and commence short-circuiting. For this very reason, the SCC design adds a second insulating component to the cell period, as illustrated in Fig. 1, where the middle layer of the sandwich-structured SCC is an electronically insulating, highly stretchable plastic. This plastic is also fully dense, unlike the MPS, and thus more robust. Unlike all-metallic CC which is both longitudinally and transversely conductive, as shown in Fig. 1, the SCC is transversely insulating, and would remain so even when deformed to the extreme. As Fig. 1 illustrates, while its longitudinal conductance is good enough in normal service, the longitudinal conductance would degrade upon stretching and mechanical abuse, due to the limited ductility of the thin metallic film (much worse than the plastic substrate) and a weaker adhesion with CAL. Thus, while SCC works well as CC in normal service, it adds significantly to
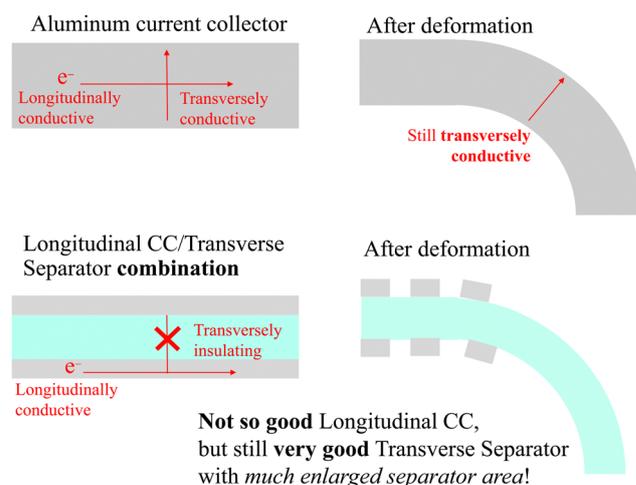

Fig. 1 Illustration of the working principle of highly stretchable SCC.

5314 | *Energy Environ. Sci.*, 2022, **15**, 5313–5323

This journal is © The Royal Society of Chemistry 2022

the "separator power" in mechanical accident scenarios due to a simple geometric effect of the increased separator area while maintaining excellent transverse insulation. In addition to sufficient longitudinal conductance, the SCC also needs to be thermomechanically robust enough as the substrate for slurry coating and CAL drying.

We prepared Al-coated polyethylene terephthalate (Al–PET) SCCs *via* a high-speed roll-to-roll process and systematically investigated their microstructure and physical properties, as well as the electrochemical performances of Al–PET SCCs-based practical pouch cells. Compared with state-of-the-art 14 μm Al CCs, we found highly competitive mechanical and electrical properties of Al–PET SCCs and cell performances, while reducing 70.4% weight and 46.4% volume. Remarkably, Al–PET SCCs effectively suppress thermal runaway events in harsh nail penetration and impact tests of fully charged pouch cells. (The same pouch cells as the one tested in Video S1 can 100% pass the nail penetration tests simply by replacing Al CCs with Al–PET SCCs, as demonstrated in Video S2 under the same, ESI†) The underlying mechanism is analyzed, and challenges regarding further development of metalized plastic CCs shall be discussed.

Film deposition, microstructure, and mechanical properties

Al layer was deposited on corona-treated PET film with a thickness of 6.0 μm *via* thermal evaporation in vacuum (Fig. S1, ESI†). The process was conducted roll-to-roll with a speed of ~5 m s^{-1} (Video S3, ESI†), and ~50 nm Al was deposited for each deposition cycle. The deposition process was repeated until the targeted thickness was reached for the Al layer. This process is highly scalable, and a roll of the obtained Al–PET SCCs (double-sided coated with Al, 0.75 μm thick on each side) is shown in Fig. S2 (ESI†). The cost of the produced Al–PET SCCs is ~5 RMB m^{-2} at present (mostly processing

cost, which can be further lowered once mass-produced). We verified that the deposited Al film is nanocrystalline and has 111 texture, as shown by X-ray diffraction (XRD) in Fig. 2a.[48] The metallic film is uniform, dense (pore-free) and fine in grain size, as shown by the cross-sectioned and top-surface scanning electron microscope (SEM) images in Fig. 2b and 1c, respectively. Under transmission electron microscope (TEM), we noted that the Al deposition has a multilayer structure (Fig. 2d) with each layer formed from an individual deposition cycle. There are many defects at the interfaces between neighboring layers (Fig. 2e), which may affect the electronic conductivity, as will be shown later. We also confirmed the good interfacial bonding between PET and Al by TEM, and it is consistent with the macroscopic Al/PET adhesion, which can survive 100 times peeling tests without noticeable changes (Fig. S3, ESI†).

The obtained Al–PET SCC has a total thickness of 7.5 μm and an areal density of 1.15 mg cm^{-2} (Table 1), which is 70.4% lighter and 46.4% thinner, and has 89.3% less metal usage than the 14 μm commercial Al CC (areal density: 3.89 mg cm^{-2}). Such reductions in weight, volume, and metal usage do not compromise mechanical properties very much. Under uniaxial tensile tests, Al–PET SCC has a modulus of 5.1 ± 0.1 GPa, a fracture strain of 92 ± 4%, and fracture strength of 196 ± 21 MPa (Fig. 2f and Table 1), compared with 14.4 ± 0.4 GPa, 3 ± 1%, and 194 ± 3 MPa for Al CC, respectively. Despite the lowered modulus, Al–PET SCC is still mechanically robust and can be successfully processed without tearing. It can be similarly handled in electrode casting, calendering, and battery assemblies as commercial Al CC. Meanwhile, there is a major difference in the fracture mode between Al (brittle fracture at ~3% strain) and Al–PET SCCs (plastically deformable up to ~90% strain, similar to uncoated PET film), which is critical for battery safety as shall be explained later.
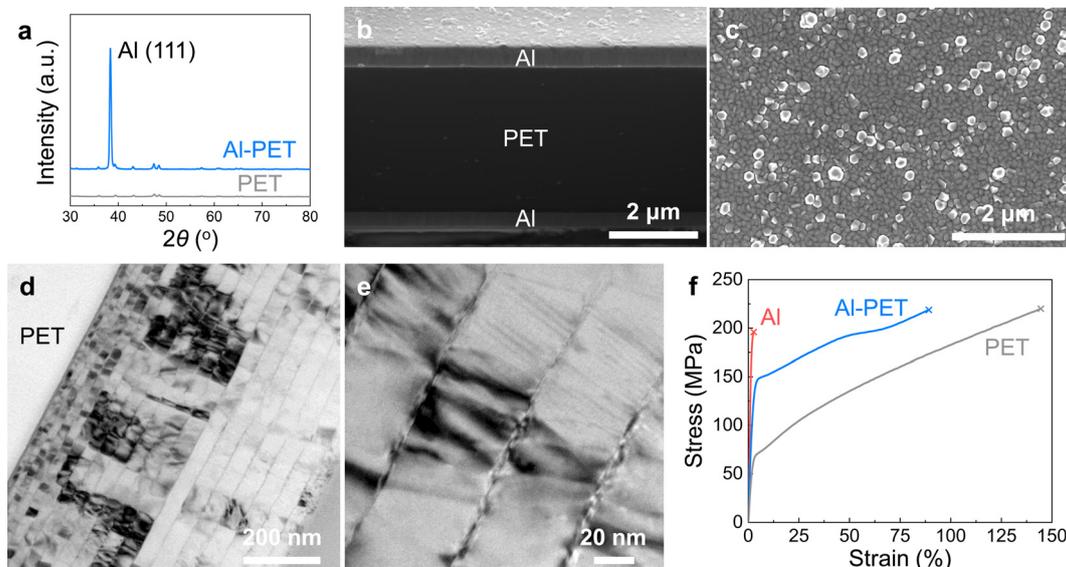

Fig. 2 Microstructure and mechanical properties of Al–PET SCCs. (a) XRD of Al–PET SCC and uncoated PET film. (b) Crossed-sectional and (c) top-surface SEM images, and (d and e) TEM images of Al–PET SCC. (f) Stress-strain curves of Al CC (thickness: 14 μm), Al–PET SCC (total thickness: 7.5 μm, with 6 μm PET and 0.75 μm Al on each side), and PET film (thickness: 6 μm).

This journal is © The Royal Society of Chemistry 2022

Energy Environ. Sci., 2022, **15**, 5313–5323 | **5315**

Table 1 Comparison of physical properties between Al and Al–PET SCCs

	Thickness (µm)	Areal density (mg cm^{-2})	Modulus (GPa)	Fracture strain (%)	Fracture strength (MPa)	Sheet resistance (mΩ □$^{-1}$)
Al	14	3.89	14.4 ± 0.4	3 ± 1	194 ± 3	2
Al–PET	7.5	1.15	5.1 ± 0.1	92 ± 4	196 ± 21	55 ± 1

Electrical properties and cell performances

The primary role of CCs is to provide long-range electronic percolation in batteries, and its ohmic loss should be minimized. To evaluate the in-plane resistance of thin films, a common measure is the sheet resistance R_s, defined as

$$R_s \equiv R\frac{W}{L} = \frac{\rho}{t}$$

where R is the resistance, L is the length, W is the width, t is the thickness, and ρ is the resistivity. The sheet resistance of Al–PET SCCs (measured by four-probe method on one side of the double-sided Al-coated PET CCs) obviously decreases with increasing Al-layer thickness (Fig. 3a; here, the thickness denotes that of the deposited Al on each side of PET). A targeted sheet resistance of <60 mΩ □$^{-1}$ can be reached for 0.75 µm and thicker Al film, which is satisfactory for most battery applications (fast charging requires further optimizations). We calculated the electrical conductivity of the deposited Al and found that it increases with thickness. The electrical conductivity of 0.75 µm thick Al is 2.42×10^7 S m^{-1}, which is 68% the electrical conductivity of the commercial 14 µm Al CCs (3.54×10^7 S m^{-1}, measured by us using the same method) and 65% the reference value of the bulk Al ($\sim3.7 \times 10^7$ S m^{-1}) (Fig. 3b).[49] The lowered electrical conductivity and its dependence on Al thickness suggest the existence of defects in the deposited nanocrystalline Al, especially in the layers deposited in earlier cycles and high-density grain boundaries, which scatter electrons in long-range transport. This is consistent with our SEM and TEM observations.

We then tested the cell performances of LiNi$_{0.5}$Co$_{0.2}$Mn$_{0.3}$O$_3$ (NCM523) cathodes with 96.2 wt% NCM523 + 3.8 wt% conductive agents and binder, on 7.5 µm Al–PET SCCs (0.75 µm Al on each side of PET) and commercial 14 µm Al CCs. For coin-type half cells against lithium metal anode, NCM523 with a mass loading of 5.0 mg cm^{-2} was one-side coated onto the cathode CCs. One corner of the Al–PET SCC was uncoated and welded with a tab for electrical contact in half cells. The half cells were tested between 2.7 and 4.2 V vs. Li$^+$/Li using Al and Al–PET SCCs, which show similar capacity and rate capability up to 2C (Fig. 3c, 1C defined as 150 mA g^{-1} for the half cells). For pouch cells, NCM523 with a mass loading of 20.8 mg cm^{-2} (on each side) was double-side coated onto the cathode CCs, corresponding to an areal capacity of ~3.22 mA h cm^{-2} on each side; for anode, graphite was double-side coated on Cu CCs with 96 wt% active material and 10 mg cm^{-2} loading on each side (corresponding to ~3.57 mA h cm^{-2} areal capacity). Pouch cells with ~244 mA h capacity were successfully assembled (more details listed in Table S1, ESI†) and tested (Fig. 3d and 2e), demonstrating that Al–PET SCCs can be robustly handled in pouch-cell preparation and assembly.

This includes successful electrode welding (inset of Fig. 3e and Fig. S4, ESI†), even though the Al layer is relatively thin. The peeling strength of the cathode (LiNi$_{0.8}$Co$_{0.1}$Mn$_{0.1}$O$_2$, polyvinylidene fluoride, Super P, and carbon nanotube with $97:1.3:1.3:0.4$ in weight ratio) on Al–PET SCCs after calendering is ~5 N m^{-1}, which is similar to ~7 N m^{-1} of the calendered cathode on Al CCs. The pouch cells using Al–PET SCCs have similar capacities and rate capability up to 2C to those using Al CCs (Fig. 3d, 1C defined as 1 h charge/discharge for the pouch cells, i.e., 244 mA for a 244 mA h pouch cell). (Thicker Al layer can be deposited for higher-rate applications. For example, increasing the Al layer thickness from 750 nm to 900 nm results in competitive rate performance with respect to 14 µm Al CC up to 4C as shown in Fig. S5, ESI†) In addition, the use of Al–PET SCCs has a negligible influence on the long-term cycling stability of the cells (Fig. 3e). Here note that Al CCs can be corroded by the by-products in organic electrolytes (e.g., HF from hydrolysis due to trace water impurities). So Al–PET SCCs should have good corrosion resistance and chemical stability. For better demonstrations, we have stored Al–PET CC in EC/DEC electrolyte (same as the electrolyte used in the present study) at 25 °C and 60 °C for 72 h. As shown in Fig. S6 (ESI†), no damage nor delamination can be observed for both samples. Based on the mass of the electrodes, the specific capacities of Al–PET electrode are $\sim5.0\%$ higher than those of Al electrode, leading to a 3.0% increase in the specific energy density at the pouch-cell level (Table S1, ESI†). Therefore, we conclude that the roll-to-roll processed Al–PET SCC has good electrical properties and cell performance, and is fully compatible with the current cathode and full-cell producing techniques to be readily used in large-capacity pouch cells.

Nail penetration tests and improved safety

In addition to the reduced weight, volume, and metal usage, Al–PET SCCs offer better safety, especially for the prevention of mechanically induced thermal runaways. To demonstrate it, we first conducted nail penetration tests of the 244 mA h pouch cells charged to 4.2 V and under 100% state of charge. (The state of charge strongly affects the thermal runaway behavior. As the state of charge increases, the self-heating reaction onsets at a lower temperature and becomes more severe, which eventually leads to combustion or even explosion of the battery.) As shown in Fig. 4a, the cell using Al CCs (in red) was quickly short-circuited (voltage dropped to 0 V) once the nail penetrates, and its temperature increased to a peak value of 69 °C measured by a thermocouple placed next to the cell. From the spatial temperature distribution in Fig. 4b (taken at ~100 s, around the peak temperature in Fig. 4a; measured by an infrared thermometer), we can see that the maximum temperature of the cell is $T_{max} = 77.8$ °C around the center position,

5316 | Energy Environ. Sci., 2022, **15**, 5313–5323

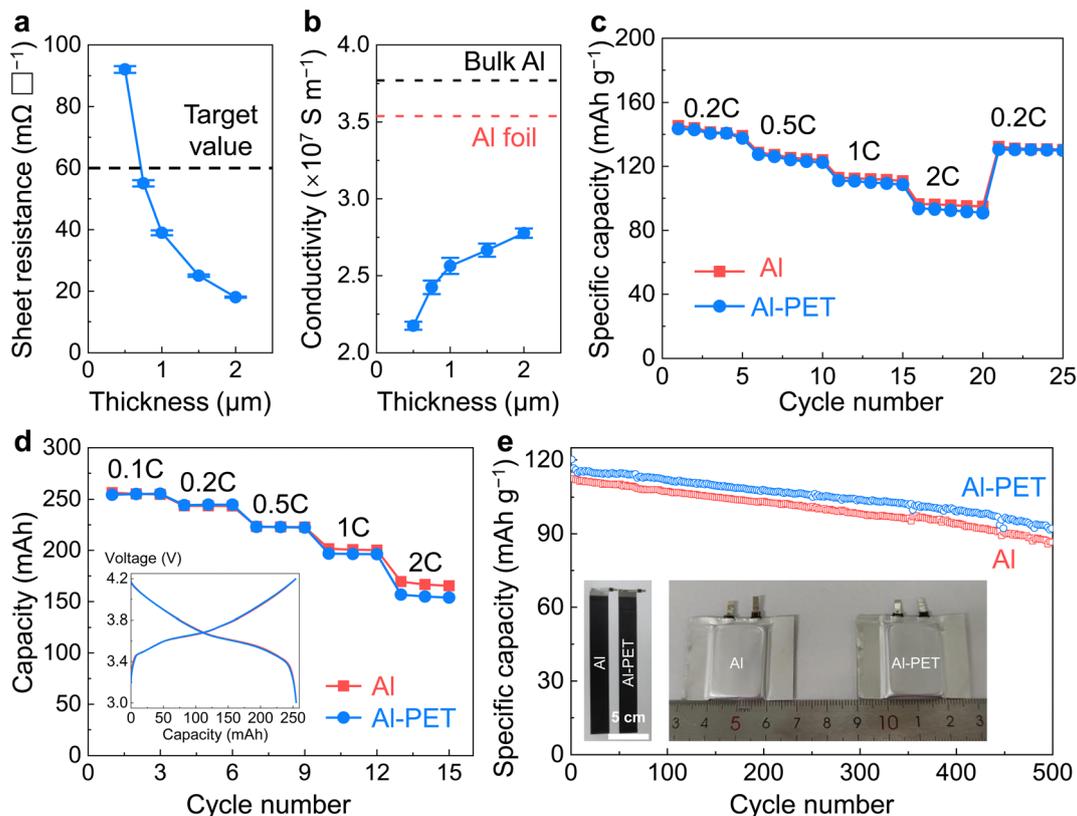This journal is © The Royal Society of Chemistry 2022

Fig. 3 Electrical properties and cell performance of Al–PET SCCs. (a) The sheet resistance of Al–PET and (b) electrical conductivity of Al film with different Al thicknesses. (c) Rate performance of coin-type half cells using Al and Al–PET SCCs between 2.7 V and 4.2 V *vs.* Li$^+$/Li. (d) Rate and (e) cycling performance of pouch cells at 1C using Al and Al–PET SCCs between 3.0 V and 4.2 V. Here, the specific capacity in (e) is calculated based on the total mass of the Al and Al–PET electrodes. Inset of (d): Charge–discharge curves of pouch cells using Al and Al–PET SCCs at 0.1C. Insets of (e): Photos of welded electrodes and assembled pouch cells using Al and Al–PET SCCs.

while the background environment temperature is $T_{en} \approx 24$ °C. In comparison, the cell using Al–PET SCCs shows stable voltage and no obvious temperature rise (Fig. 4a, in blue) during the nail penetration test. The mapped temperature distribution in Fig. 4c demonstrates that the cell using Al–PET SCCs has spatially uniform temperatures close to $T_{en} \approx 24$ °C.

Similarly suppressed short-circuiting and temperature rise by Al–PET SCCs were also observed in impact tests of the 244 mA h pouch cells under 100% state of charge (Fig. S7, ESI†). Since the thermal runaway event depends on the capacity and cathode/anode chemistry of the pouch cells, we further investigated the effect of Al–PET SCCs in 4.3 A h pouch cells (1C defined as 1 h charge/discharge for the pouch cells, *i.e.*, 4300 mA for a 4300 mA h pouch cell) using LiNi$_{0.8}$Co$_{0.1}$Mn$_{0.1}$O$_2$ (NCM811) cathode and hybrid graphite@SiO anode (Fig. S8 and Table S2, ESI†). As shown by Video S1 (ESI†), cells using Al CCs under 100% state of charge quickly caught fire and exploded as the nail penetrated. In comparison, the cells using Al–PET SCCs under 100% state of charge can pass the nail penetration tests without fire or smoke (Fig. S9 and Videos S2, ESI†).

Mechanisms for improved safety

To understand the mechanism behind the improved safety, we first noted the well-preserved voltage profile and normal

charge/discharge curves of the pouch cell using Al–PET SCCs after the nail penetration test (Fig. 4d), which indicates that the penetrated region was electronically isolated from the rest of the stack. The key to safety is how to prevent a sharp increase in the local electronic conductance upon penetration, despite many new opportunities for mechanical contacts to form between Al, Cu, cathode-active layer (NCM + conductive agents), anode-active layer (graphite + conductive agents), and the penetrant itself, when these layers are all severely deformed and penetrated. Our observations led us to focus on the coupled electrical-mechanical properties of calendered cathodes on Al–PET SCCs (double-side coated in assembled pouch cells) and how they can improve battery safety.

We first conducted electrical measurements during uniaxial tests of the Al–PET SCCs and the cathodes. For Al–PET SCCs without cathode-active layer, we found its resistance gradually increases with applied tensile strain (Fig. 5a), until Al–PET SCCs break at ∼80% strain. It is despite the fact that many micro-cracks in the Al layer can be observed at the surface of Al–PET SCCs (Fig. 5b–d), which are resistive but do not completely stop long-range electronic percolation. This proves there is strong interfacial bonding between Al and PET, which takes advantage of the large uniform ductility of PET and prevents strain localization in Al for "brittle" fracture (Fig. 2f). Such a

This journal is © The Royal Society of Chemistry 2022

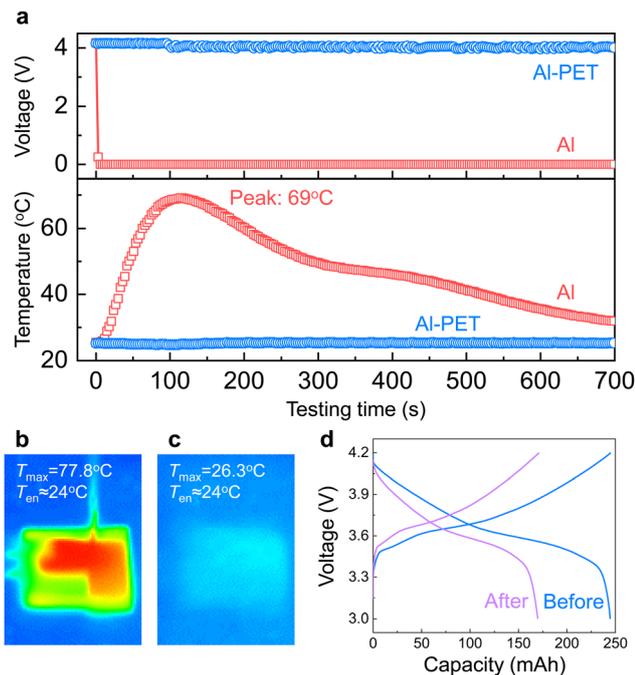*Energy Environ. Sci.*, 2022, **15**, 5313–5323 | **5317**

Fig. 4 Al–PET SCCs suppress short-circuiting and temperature rise in nail penetration tests. (a) Voltage and temperature (measured by a thermocouple) of 244 mA h pouch cells using Al and Al–PET SCCs during nail penetration tests. (b and c) Temperature distributions (measured by an infrared thermometer) of the cells using (b) Al and (c) Al–PET SCCs around the peak temperature points in (a). (d) Voltage-capacity curves of the cell using Al–PET SCCs before and after nail penetration test.

mechanical behavior is beneficial for processing and handling Al–PET SCCs, including cell preparation and assembly, where in-plane electronic percolation needs to be guaranteed for normal handling. For both uncoated Al CCs and calendered cathodes on Al CCs, we found a brittle fracture at ∼3% tensile strain (Fig. S10, ESI†) and the cathodes were still adhered to Al CCs after fracture (Video S4, ESI†). This comparison is somewhat counter-intuitive, since one could say in this narrow sense that Al CC should act more like "mechanical fuse" than Al–PET SCC, which upon stretching, would break the electronic connection like circuit breakers and fuses. The fact that Al–PET SCC can sustain ∼80% tensile strain without losing in-plane electronic percolation is quite astonishing, that does not seem to help stop local short-circuiting like ADS (Automatic Disconnection of Supply) safety devices do. We note, however, that Fig. 5 only subjects the CCs to simple in-plane stretch strain pattern without bending. Nevertheless, we confirmed the high ductile and deformable nature of PET film, which translates to Al–PET SCCs. Under extreme straining conditions, we expect the plastically deformable and electronically insulating PET can wrap around sharp edges of electronically conductive elements, and the Al layer can also be severely cracked to stop long-range electronic percolation to the nail penetrated region.

For calendered cathodes on Al–PET SCCs, they can be plastically deformed up to ∼60% tensile strain (Fig. S10, ESI†) with gradually increasing resistance. However, we noted that only the Al–PET SCCs were deformed, but not the coated cathode. As shown in Fig. 5f–i and Video S5 (ESI†), while the width of the Al–PET SCCs decreases as tensile strain increases, there is little change in the width of the cathode-active layer. Instead, many transverse cracks are formed in the cathode-active layer, which clearly delaminates from the Al–PET SCC and finally falls off (Fig. 5i). This indicates a weak interface between the coated cathode layer and the Al layer of Al–PET SCCs, which results in effective delamination upon straining (Fig. 5j). This would add to the electrically and thermally insulating volume fraction (occupied by the vacuum) and isolate the CAL fragments in electrical and thermal senses from the other active parts around the nail penetrated region, preventing them from further chemically fueling the local thermal runaway. Fundamentally, this arises out of the large mismatch in deformability between the PET polymer and the cathode-active layer. In the literature, Pham *et al.* previously attributed the electrical isolation of cathode materials during mechanical abuse to the shrinkage of the polymer substrate (which shrinks upon heating).[32] This does not apply to our cases as no obvious temperature increase was detected (Fig. 4a–c and Fig. S7, S9, ESI†). Therefore, our Al–PET SCCs offer transverse insulation mechanically before the thermal abuse loop is entered.

We next performed X-ray micro-computed tomography (CT) measurements on the nail-penetrated pouch cells. Around the penetration spot, we observed huge deformations of all components in the cell (CCs, CAL, anode, separator), where all layers get damaged, deformed, and entangled. The fly-by 3D movie is shown in Video S6–S9 (ESI†). It is clear that the strain pattern is hugely complex, with tremendous bending and distortions, and far beyond the simple in-plane stretching shown in Fig. 5. The fracture of Al, Cu, CAL (NCM + conductive agents), anode-active layer (graphite + conductive agents) leaves many jagged edges, that could lead to electronic short-circuiting. It is therefore possible for cathode and anode to become in direct contact (across broken separator), cathode and anode CCs in direct contact (cutting through separator by sharp metal edges), as well as cathode/anode CC with the metallic penetrant. For the cells using Al CCs, while CAL segments showing brittle fracture were observed, they still adhered to the Al CCs so electronic percolation is maintained (Fig. 6a–d and Video S6, S7, ESI†) – note that the metallic penetrant, if not wrapped, can directly connect multiple vertical layers and thus reduce the stringent requirement on longitudinal electronic percolation in Fig. 1. Electrochemically or Joule-heating driven degradation such as oxygen release from the local CAL fragment may continue at a locally elevated temperature, as long as the CAL fragment is still adherent to something metallic and hot, fueling local thermal runaway. For the cells using Al–PET SCCs, we observed plastically deformed Al–PET SCCs and effectively detached cathodes from Al–PET SCCs (Fig. 6e–h and Video S8, S9, ESI†). This supports our hypothesis that highly deformable PET can wrap around sharp edges of electronically conductive elements and cut off the abused internal electrical circuit (also due to decohesion with CAL), just like an accident-activated transverse "separator" (Fig. 7). In comparison,
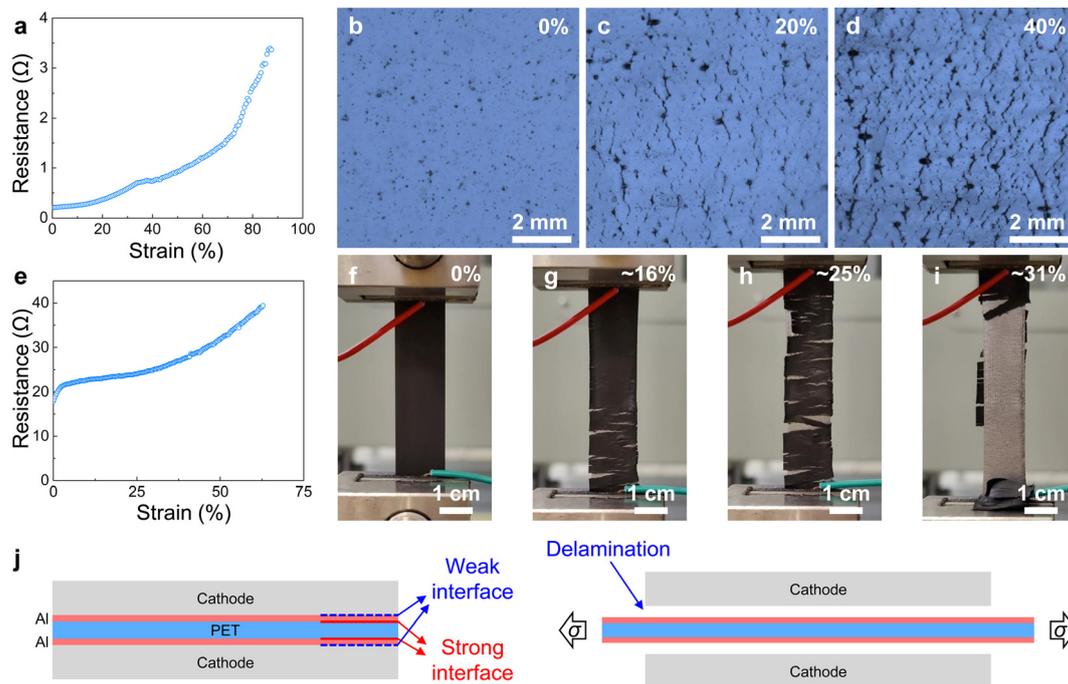
5318 | *Energy Environ. Sci.*, 2022, **15**, 5313–5323

This journal is © The Royal Society of Chemistry 2022

Fig. 5 Response of Al−PET SCCs and cathodes under strain. (a) Resistance−strain curve of Al−PET SCCs. (b−d) Optical images of Al−PET SCCs under (b) 0%, (c) 20%, and (d) 40% tensile strain. (e) Resistance−strain curve of calendered cathodes (NCM523 double-sided coated on Al−PET SCCs). (f−i) Photos of cathodes under (f) 0%, (g) ∼16%, (h) ∼25%, and (i) 31% tensile strain. (j) Schematic mechanism for cathode delamination from Al−PET SCCs under strain.
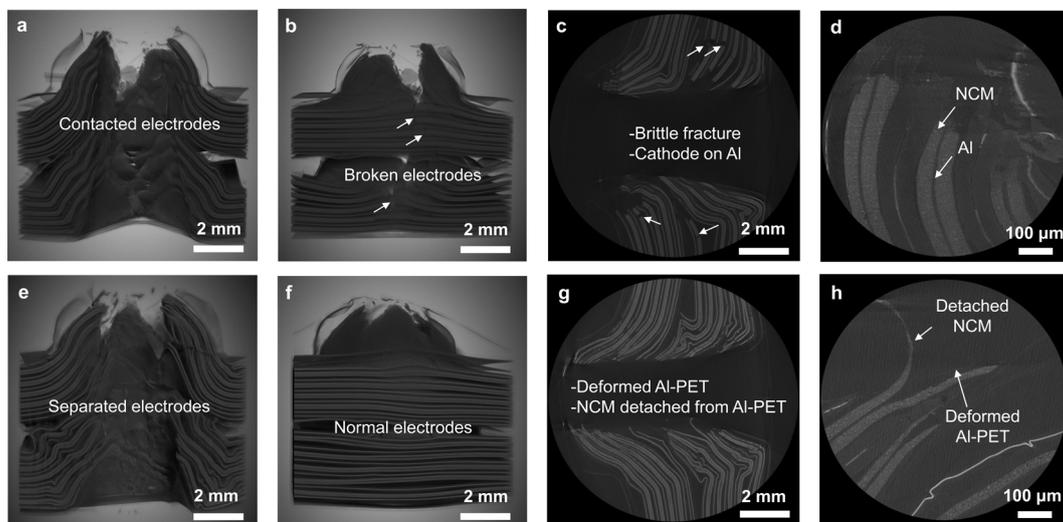

Fig. 6 Different deformation and fracture behaviors between Al and Al−PET SCCs. X-ray micro-CT images around the penetration spots for the nail-penetrated pouch cells using (a−d) Al and (e−h) Al−PET SCCs.

while the polyethylene (PE) separator offers good insulation between anode and cathode under normal battery operations, it is not very deformable and cannot contribute much to safety in mechanically abused events. (PE separator shrinks upon heating, such as in early stage of thermal runaway, which reduces "separating power") Therefore, the new functionality of Al−PET SCCs as in-service "separators" for mechanically abused events is critical to the improved safety. The local CAL is effectively delaminated from Al−PET SCCs and becomes inactive. This would electrically

and thermally isolate the local CAL segments from hot metals, which minimizes the production of oxygen gas or radicals, cutting off chemical fueling of the local thermal runaway.

Diagnosing short-circuiting pathways during penetration accidents

We further conducted control experiments to compare the short-circuiting behaviors of various cell configurations during penetration tests using both electrically conductive stainless
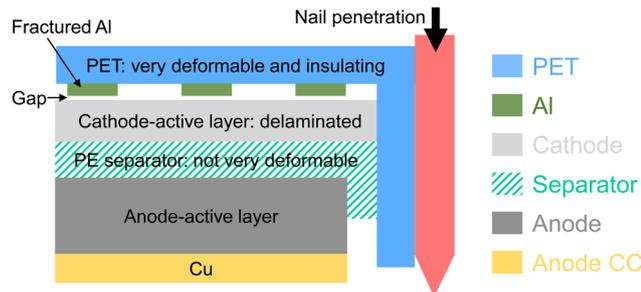
Fig. 7 Schematic deformation map during nail penetration tests.

steel nail and insulating glass nail: (a) for "standard" cells (using NCM523 cathode and graphite anode under 100% state of charge, same as in the previous section), the ones using Al CCs short-circuited when penetrated with either stainless steel or glass nails (Fig. S11, ESI†), while the ones using Al–PET SCCs did not in either case. (b) For the cells same as (a) but without adding liquid electrolyte, the cells using Al CCs are under open circuit condition before nail penetration tests. However, the cell resistance decreased to $58 \pm 25\ \Omega$ after the stainless-steel nail penetrated and to $298 \pm 82\ \Omega$ after the stainless-steel nail was pulled out. When using glass nail, the cell resistance similarly decreased, to $24 \pm 4\ \Omega$ after the nail penetrated and to $37 \pm 9\ \Omega$ after the nail was pulled out (Table S3, ESI†). In comparison, for both stainless steel and glass nails, the cells using Al–PET SCCs are under open circuit condition before nail penetration and have very large resistance over $5000\ \Omega$ after nail penetration and pullout. (c) For "cells" consisted of rolled multilayer cathode CCs (Al or Al–PET) and anode CCs (Cu), both coated with insulating Al_2O_3 but without active cathode/anode materials nor liquid electrolyte, the cells using Al CCs are under open circuit condition before nail penetration. However, the cell resistance again decreased when stainless steel or glass nail penetrated and was pulled out (Table S4, ESI†). In comparison, for both stainless steel and glass nails, the cells using Al–PET SCCs were always under open circuit condition before nail penetration as well as after nail penetration and pullout.

The detailed mechanisms can now be analyzed, and we shall consider three possible pathways for short-circuiting (Fig. 8): Path 1, from cathode CCs to electrically conductive nail to anode CCs; Path 2, from cathode CCs to cathode to anode to anode CCs (which happens when separate is damaged and the

cathode and the anode are in direct contact); Path 3, directly from cathode CCs to anode CCs (when the two sides are in direct contact). From the comparison in (a) for stainless steel *vs.* glass nail, it is clear that Path 1 contributes to minor short-circuiting current (the Path 1 does not exist when glass nail was used). From the experiments for the cells using Al CCs in (b and c), both Path 2 and 3 play major roles in short-circuiting. In comparison, Al–PET SCCs can mitigate short-circuiting events as shown by the experiments in (a–c), because: Path 1 is suppressed due to thinner Al layer thickness, thus much less contact area with the nail; Path 2 is suppressed due to delaminated cathodes from Al–PET SCCs, leaving a gap in between; Path 3 is suppressed due to plastically deformed PET substrates, which effectively wrap around fractured metallic Al or Cu that can have a sharp edge. In addition, we mentioned the transverse cracks in the CAL layer, which would also help cut down cross-talk with the CAL and CCs over longer distances.

Conclusions and outlook

To summarize, we systematically investigated the microstructure, electrical and mechanical properties, and cell performance of roll-to-roll processed, mass-produced Al–PET SCCs. Their application in batteries effectively lowers the weight, volume, and metal usage of the cathode CCs without sacrificing any major battery performance. More importantly, battery safety is remarkably improved, where fully charged high-energy-density batteries can now pass harsh nail penetration and impact tests. The underlying mechanisms were analyzed, and the key lies in the mechanically deformable polymer substrate (serving as an accident-active separator for mechanically abused events) as well as the matched/mismatched interfaces (a strong Al/PET interface and a weak cathode/Al–PET interface). While the safety benefits do initially come as a side product as we thin down the CCs, it also points out the importance of processing optimizations and the possibility of having smart, multi-functional CCs for better batteries. Looking forward, several key issues still need to be solved scientifically and technologically, including (a) how to eliminate processing defects and further improve electronic conductivity of the deposited Al film, (b) how to further lower sheet resistance to enable fast charging, (c) how to further improve the interfacial bonding between Al and polymer substrate to avoid delamination/degradation during aging in highly corrosive electrolytes (*e.g.*, containing HF), and (d) what other new functions may be simultaneously integrated in the cathode and anode CCs.

Methods

Preparation of Al–PET SCCs

Al film was deposited layer-by-layer *via* thermal evaporation on commercial corona-treated PET films (6 μm thick; XR41H, Toray Co. LTD; Table S5, ESI†) in a roll-to-roll process (rolling speed: ~5 m s^{-1}) under vacuum evaporation machine (chamber pressure: ~1.8 Pa; Applied Materials Inc., USA, Applied Top Met). The temperature of the evaporation boat was controlled up to
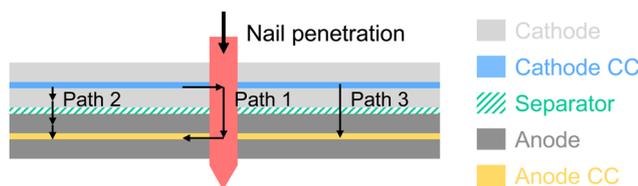
Short-circuiting pathways:
1. Cathode CC → nail →anode CC (minor)
2. Cathode CC → cathode → anode → anode CC (major)
3. Directly contacted cathode and anode CCs (major)

Fig. 8 Schematic short-circuiting pathways during nail penetration tests.

5320 | *Energy Environ. Sci.*, 2022, **15**, 5313–5323

This journal is © The Royal Society of Chemistry 2022

1500 °C by adjusting the applied voltage. The melted Al wires were vaporized and deposited on the surface of the PET. For each deposition cycle, a layer of Al with $\sim$50 nm thickness was deposited, and the deposition process was repeated until a targeted thickness of the Al layer was reached.

Characterizations

SEM images were taken under a Helios G4 UX Dual Beam scanning electron microscope. TEM images were taken under a JEM-2100F transmission electron microscope. XRD measurements were conducted on a D8 Advance X-ray diffractometer with monochromator-filtered Cu K_α radiation. Conductivity measurements were conducted by a four-point probe method (DMR-1C, Daming instrument). Uniaxial tensile tests were conducted on trimmed samples (length: 100 mm, width: 15 mm) using a micro materials tester (WANCE, Shenzhen, China) under a rate of 10 mm min^{-1}. Measured sample resistance during tensile tests was recorded by an electrochemical workstation (Interface 1010, Gamry). X-ray micro-CT measurements were conducted on Zeiss Xradia 515 Versa X-ray microscopes (Carl Zeiss) under a scanning energy of 140 kV/10 W. Samples were mounted on the holder with an aluminum adapter and rotated horizontally by 180°, then paused at discrete angles to collect 2-dimensional projection images.

Cell preparation, assembly, and testing

To prepare cathode slurry, NCM523, carbon nanotubes (CNT), conductive carbon (Super P), and polyvinylidene fluoride (PVDF) were mixed with 96.2 : 0.6 : 1.6 : 1.6 in weight ratio using N-methyl-2-pyrrolidone (NMP) as the solvent. Al and Al–PET SCCs were one-side coated with an NCM523 loading of 5.0 mg cm^{-2} for coin cells and double-side coated with an NCM523 loading of 20.8 mg cm^{-2} (per side) for 244 mA h pouch cells. For coin cells, one corner of the Al–PET SCCs was left uncoated and welded for electrical contact. For coin cells, lithium foil was used as the anode, and 1 M LiPF$_6$ in 1 : 1 (vol : vol) ethylene carbonate/diethyl carbonate (EC/DEC) with 5% fluoroethylene carbonate (FEC) additive was used as the electrolyte. Coin cells were tested under a voltage range of 2.7 V to 4.2 V using a battery testing system (CT-4000, Neware). To prepare anode slurry for 244 mA h pouch cells, graphite, conductive carbon (Super P), carboxymethyl cellulose (CMC), and styrene-butadiene rubber (SBR) were mixed with 96 : 1.5 : 1.3 : 1.2 in weight ratio using water as the solvent. Cu CCs were double-side coated with a graphite loading of 10 mg cm^{-2} (per side). 4.3 A h pouch cells were prepared using NCM811 as the cathode materials and graphite/SiO as the anode materials. The cathode electrode (21.1 mg cm^{-2} per side) consists of the NCM811, PVDF, Super P, and CNT with 97 : 1.3 : 1.3 : 0.4 in weight ratio. The anode electrode (8.3 mg cm^{-2} per side) consists of the SiO (15 wt%)/graphite, Super P, CMC, and SBR with 95.9 : 1.1 : 1 : 2 in weight ratio. For all the pouch cells, 1 M LiPF$_6$ in 1 : 1 : 1 (vol : vol : vol) ethylene carbonate/dimethyl carbonate/ethyl methyl carbonate (EC/DMC/EMC) with 1% vinylene carbonate (VC) additive was used as the electrolyte. Ceramic-coated polyethylene film was used as the separator for all the cells.

Ultrasonic spot-welding machine (Guangzhou KEPU Ultrasonic Electronic Technological Co. LTD) was used to weld the CCs to the Al tabs. For Al–PET SCCs, the voltage, time, and air pressure of welding of were set, respectively, to 120 V, 1 s, and 0.6 MPa. While the parameters were 65 V, 0.3 s, and 0.2 MPa for Al CCs.

Nail penetration tests

Nail penetration tests were conducted on DMS-ZC Nail-Penetration Tester (Damsion, Shenzhen, China). A stainless-steel or glass nail was penetrated through the pouch cell at a speed of 10 mm s^{-1}. (4 mm nail was used for the penetration test of the 244 mA h cells and 8 mm nail was used for the penetration test of the 4300 mA h cells.) The tested pouch cells were charged to 4.2 V and 100% state of charge before the nail penetration tests. Voltages and temperatures (measured separately by a nearby thermocouple and an infrared thermometer) were recorded during nail penetration tests. The thermocouple used is a K-type thermocouple (compensation wire: 2 $\times$ 0.4 mm, temperature range: -70 to 850 °C) equipped on the Nail-Penetration Tester. In the experiments, the thermocouple was attached to the surface of the battery by a tape to monitor the temperature.

Impact tests

Impact tests were conducted on GX-5066-NE Impact Tester (Dongguan, China). The pouch cell was placed on a flat surface. A steel rod (diameter: 15.8 mm) was placed on top of the pouch cell. An impact (weight: 9.1 kg) then fell freely from a position of 610 mm higher and onto the steel rod. The tested 244 mA h pouch cells (with NCM523 cathodes) were charged to 4.2 V and 100% state of charge before impact tests. Voltages and temperatures (measured by a nearby thermocouple) were recorded during impact tests.

Author contributions

Z. Liu, Y. Dong, L. Qie, J. Li, and Y. Huang conceived the concept and designed the experiments. Z. Liu conducted material characterizations, battery assembly, and electrochemical measurements. Z. Liu, Y. Dong, and L. Qie analyzed the data. X. Qi, Z. Zhu, R. Wang, and C. Yan contributed to the fabrication of pouch cells. X. Jiao contributed to the production of roll-to-roll processed Al–PET. Z. Liu, Y. Dong, L. Qie, J. Li, and Y. Huang wrote the paper. All authors discussed and contributed to the writing.

Conflicts of interest

The authors declare no competing interests.

Acknowledgements

This journal is © The Royal Society of Chemistry 2022

Energy Environ. Sci., 2022, **15**, 5313–5323 | 5321

References

1 Z. Chen, P. Hsu, J. Lopez, Y. Li, J. W. F. To, N. Liu, C. Wang, S. C. Andrews, J. Liu, Y. Cui and Z. Bao, *Nat. Energy*, 2016, **1**, 1–2.

2 Z. Gao, H. Sun, L. Fu, F. Ye, Y. Zhang, W. Luo and Y. Huang, *Adv. Mater.*, 2018, **30**, 1705702.

3 F. Duffner, N. Kronemeyer, J. Tübke, J. Leker, M. Winter and R. Schmuch, *Nat. Energy*, 2021, **6**, 1–12.

4 R. Choudhury, J. Wild and Y. Yang, *Joule*, 2021, **5**, 1301–1305.

5 H. Maleki, S. Hallaj, J. R. Selman, R. B. Dinwiddie and H. Wang, *J. Electrochem. Soc.*, 1999, **146**, 947–954.

6 S. Jin, Y. Jiang, H. Ji and Y. Yu, *Adv. Mater.*, 2018, **30**, 1802014.

7 B. Rieger, S. Schlueter, S. V. Erhard, J. Schmalz, G. Reinhart and A. Jossen, *J. Energy Storage*, 2016, **6**, 213–221.

8 P. Zhu, D. Gastol, J. Marshall, R. Sommerville, V. Goodship and E. Kendrick, *J. Power Sources*, 2021, **485**, 229321.

9 M. Wang, W. Yao, P. Zou, S. Hu, H. Zhu, K. Liu and C. Yang, *J. Power Sources*, 2021, **490**, 229527.

10 N. Li, Z. Chen, W. Ren, F. Li and H.-M. Cheng, *Proc. Natl. Acad. Sci. U. S. A.*, 2012, **109**, 17360–17365.

11 H. Sun, J. Zhu, D. Baumann, L. Peng, Y. Xu, I. Shakir, Y. Huang and X. Duan, *Nat. Rev. Mater.*, 2019, **4**, 45–60.

12 L. Lu, J. T. M. De Hosson and Y. Pei, *Carbon*, 2019, **144**, 713–723.

13 X. Liu, D. Chao, D. Su, S. Liu, L. Chen, C. Chi, J. Lin, Z. X. Shen, J. Zhao, L. Mai and Y. Li, *Nano Energy*, 2017, **37**, 108–117.

14 Y. Chen, K. Fu, S. Zhu, W. Luo, Y. Wang, Y. Li, E. Hitz, Y. Yao, J. Dai, J. Wan, V. A. Danner, T. Li and L. Hu, *Nano Lett.*, 2016, **16**, 3616–3623.

15 A. L. M. Reddy, A. Srivastava, S. R. Gowda, H. Gullapalli, M. Dubey and P. M. Ajayan, *ACS Nano*, 2010, **4**, 6337–6342.

16 H. Zhang, X. Yu and P. V. Braun, *Nat. Nanotechnol.*, 2011, **6**, 277–281.

17 Y.-Q. Li, J.-C. Li, X.-Y. Lang, Z. Wen, W.-T. Zheng and Q. Jiang, *Adv. Funct. Mater.*, 2017, **27**, 1700447.

18 H. Zhang and P. V. Braun, *Nano Lett.*, 2012, **12**, 2778–2783.

19 B. Liu, J. Zhang, X. Wang, G. Chen, D. Chen, C. Zhou and G. Shen, *Nano Lett.*, 2012, **12**, 3005–3011.

20 S. W. Kim and K. Y. Cho, *J. Electrochem. Sci. Technol.*, 2015, **6**, 1–6.

21 D. Chen, Y. Zhang, T. Bessho, J. Sang, H. Hirahara, K. Mori and Z. Kang, *Chem. Eng. J.*, 2016, **303**, 100–108.

22 L. A. C. Teixeira and M. C. Santini, *J. Mater. Process. Technol.*, 2005, **170**, 37–41.

23 C. A. Bishop, *Multilayer Flexible Packaging*, Elsevier, 2016.

24 H. Mohammadhosseini, R. Alyousef, N. H. Abdul Shukor Lim, M. M. Tahir, H. Alabduljabbar, A. M. Mohamed and M. Samadi, *J. Cleaner Prod.*, 2020, **258**, 120726.

25 M. Makdessi, A. Sari and P. Venet, *Microelectron. Reliab.*, 2014, **54**, 1823–1827.

26 M. Rabuffi and G. Picci, *IEEE Trans. Plasma Sci.*, 2002, **30**, 1939–1942.

27 W. Zhang, Y. C. Wei, M. X. Cheng, Y. M. Liu and H. Sun, *Eng. Failure Anal.*, 2021, **120**, 105036.

28 N. Semaltianos, *Appl. Surf. Sci.*, 2001, **183**, 223–229.

29 S. Gupta, M. Dixit, K. Sharma and N. S. Saxena, *Surf. Coat. Technol.*, 2009, **204**, 661–666.

30 K. Mueller, C. Schoenweitz and H.-C. Langowski, *Packag. Technol. Sci.*, 2012, **25**, 137–148.

31 B. G. Morin and C. C. Hu, *US Pat.*, 15/927,078, 2018.

32 M. T. M. Pham, J. J. Darst, W. Q. Walker, T. M. M. Heenan, D. Patel, F. Iacoviello, A. Rack, M. P. Olbinado, G. Hinds, D. J. L. Brett, E. Darcy, D. P. Finegan and P. R. Shearing, *Cell Rep. Phys. Sci.*, 2021, **2**, 100360.

33 Y. Ye, L.-Y. Chou, Y. Liu, H. Wang, H. K. Lee, W. Huang, J. Wan, K. Liu, G. Zhou, Y. Yang, A. Yang, X. Xiao, X. Gao, D. T. Boyle, H. Chen, W. Zhang, S. C. Kim and Y. Cui, *Nat. Energy*, 2020, **5**, 786–793.

34 T. T. D. Nguyen, S. Abada, A. Lecocq, J. Bernard, M. Petit, G. Marlair, S. Grugeon and S. Laruelle, *World Electr. Veh. J.*, 2019, **10**, 79.

35 R. Xiong, S. Ma, H. Li, F. Sun and J. Li, *iScience*, 2020, **23**, 101010.

36 H. Wu, D. Zhuo, D. Kong and Y. Cui, *Nat. Commun.*, 2014, **5**, 5193.

37 K. Liu, W. Liu, Y. Qiu, B. Kong, Y. Sun, Z. Chen, D. Zhuo, D. Lin and Y. Cui, *Sci. Adv.*, 2017, **3**, e1601978.

38 K. Liu, Y. Liu, D. Lin, A. Pei and Y. Cui, *Sci. Adv.*, 2018, **4**, eaas9820.

39 W. Li, E. M. Erickson and A. Manthiram, *Nat. Energy*, 2020, **5**, 26–34.

40 M. Yoon, Y. Dong, J. Hwang, J. Sung, H. Cha, K. Ahn, Y. Huang, S. J. Kang, J. Li and J. Cho, *Nat. Energy*, 2021, **6**, 362–371.

41 W. Xue, M. Huang, Y. Li, Y. G. Zhu, R. Gao, X. Xiao, W. Zhang, S. Li, G. Xu, Y. Yu, P. Li, J. Lopez, D. Yu, Y. Dong, W. Fan, Z. Shi, R. Xiong, C.-J. Sun, I. Hwang, W.-K. Lee, Y. Shao-Horn, J. A. Johnson and J. Li, *Nat. Energy*, 2021, **6**, 495–505.

42 U.-H. Kim, G.-T. Park, B.-K. Son, G. W. Nam, J. Liu, L.-Y. Kuo, P. Kaghazchi, C. S. Yoon and Y.-K. Sun, *Nat. Energy*, 2021, **6**, 115.

43 O. S. Mendoza-Hernandez, H. Ishikawa, Y. Nishikawa, Y. Maruyama and M. Umeda, *J. Power Sources*, 2015, **280**, 499–504.

44 T. Ma, L. Chen, S. Liu, Z. Zhang, S. Xiao, B. Fan, L. Liu, C. Lin, S. Ren and F. Wang, *J. Power Sources*, 2019, **437**, 226928.

5322 | *Energy Environ. Sci.*, 2022, **15**, 5313–5323

This journal is © The Royal Society of Chemistry 2022

45 L. M. Cederberg. Cederberg law: Oct. 20, 2021; **https://cederberglaw.com/how-many-car-accidents-will-i-have-in-my-lifetime/**.

46 F. Lambert. Electrek: Oct. 20, 2021; **https://electrek.co/2021/04/26/tesla-releases-more-details-fatal-crash-in-texas-but-questions-unanswered/**.

47 P. Arora and Z. Zhang, *Chem. Rev.*, 2004, **104**, 4419–4462.

48 J. Gu, B. Li, Z. Du, C. Zhang, D. Zhang and S. Yang, *Adv. Funct. Mater.*, 2017, **27**, 1700840.

49 A. Zameshin, M. Popov, V. Medvedev, S. Perfilov, R. Lomakin, S. Buga, V. Denisov, A. Kirichenko, E. Skryleva, E. Tatyanin, V. Aksenenkov and V. Blank, *Appl. Phys. A: Mater. Sci. Process.*, 2012, **107**, 863–869.

This journal is © The Royal Society of Chemistry 2022

Energy Environ. Sci., 2022, **15**, 5313–5323 | **5323**